AFRL-AFOSR-VA-TR-2016-0362

A Posteriori Quantification of Rate-Controlling Effects from High-Intensity Turbulence-Flame Interactions Using 4D Measurements

ADAM STEINBERG
UNIVERSITY OF TORONTO
27 KINGS COLEGE CIR
TORONTO, 21421016
CA

11/22/2016
Final Report

REPORT DOCUMENTATION PAGE

Form Approved
OMB No. 0704-0188

The public reporting burden for this collection of information is estimated to average 1 hour per response, including the time for reviewing instructions, searching existing data sources, gathering and maintaining the data needed, and completing and reviewing the collection of information. Send comments regarding this burden estimate or any other aspect of this collection of information, including suggestions for reducing the burden, to Department of Defense, Executive Services, Directorate (0704-0188). Respondents should be aware that notwithstanding any other provision of law, no person shall be subject to any penalty for failing to comply with a collection of information if it does not display a currently valid OMB control number.
PLEASE DO NOT RETURN YOUR FORM TO THE ABOVE ORGANIZATION.

1. REPORT DATE *(DD-MM-YYYY)*	2. REPORT TYPE	3. DATES COVERED *(From - To)*
22-11-2016	Final Performance	15 Jan 2013 to 14 Jan 2016

4. TITLE AND SUBTITLE
A Posteriori Quantification of Rate-Controlling Effects from High-Intensity Turbulence-Flame Interactions Using 4D Measurements

5a. CONTRACT NUMBER

5b. GRANT NUMBER
FA9550-13-1-0070

5c. PROGRAM ELEMENT NUMBER
61102F

6. AUTHOR(S)
ADAM STEINBERG

5d. PROJECT NUMBER

5e. TASK NUMBER

5f. WORK UNIT NUMBER

7. PERFORMING ORGANIZATION NAME(S) AND ADDRESS(ES)
UNIVERSITY OF TORONTO
27 KINGS COLEGE CIR
TORONTO, 21421016 CA

8. PERFORMING ORGANIZATION REPORT NUMBER

9. SPONSORING/MONITORING AGENCY NAME(S) AND ADDRESS(ES)
AF Office of Scientific Research
875 N. Randolph St. Room 3112
Arlington, VA 22203

10. SPONSOR/MONITOR'S ACRONYM(S)
AFRL/AFOSR RTA1

11. SPONSOR/MONITOR'S REPORT NUMBER(S)
AFRL-AFOSR-VA-TR-2016-0362

12. DISTRIBUTION/AVAILABILITY STATEMENT
DISTRIBUTION A: Distribution approved for public release.

13. SUPPLEMENTARY NOTES

14. ABSTRACT
This project addressed variations in the chemical reaction rate as high-intensity turbulence interacts with premixed combustion fronts. Specically, we aimed to experimentally quantify local reaction rate, and relate this to the local thermo-chemical structure. These objectives were achieved by simultaneous application of various high-speed laser-based measurement techniques in a series of piloted premixed jet ames, which were capable of achieving high Karlovitz numbers and low Damkohler numbers in a tractable and repeatable manner. Several advancements also were made in the areas of laser diagnostics and data-mining techniques.

15. SUBJECT TERMS
Combustion, Turbulence, diagnostics

16. SECURITY CLASSIFICATION OF:			17. LIMITATION OF ABSTRACT	18. NUMBER OF PAGES	19a. NAME OF RESPONSIBLE PERSON
a. REPORT	b. ABSTRACT	c. THIS PAGE			LI, CHIPING
Unclassified	Unclassified	Unclassified	UU		

19b. TELEPHONE NUMBER *(Include area code)*
703-696-8574

Standard Form 298 (Rev. 8/98)
Prescribed by ANSI Std. Z39.18

Final Report: A Posteriori Quantification of Rate-Controlling Effects from High-Intensity Turbulence-Flame Interactions Using 4D Measurements

Adam M. Steinberg

Institute for Aerospace Studies

University of Toronto

Toronto, ON, Canada, M3H 5T6

July 6, 2016

1 Overview

This project addressed variations in the chemical reaction rate as high-intensity turbulence interacts with premixed combustion fronts. Specifically, we aimed to experimentally quantify local reaction rate, and relate this to the local thermo-chemical structure. These objectives were achieved by simultaneous application of various 'high-speed' laser-based measurement techniques in a series of piloted premixed jet flames, which were capable of achieving high Karlovitz numbers and low Damköhler numbers in a tractable and repeatable manner. Several advancements also were made in the areas of laser diagnostics and data-mining techniques. Major conclusions and accomplishments include:

1. We demonstrated the first application of high-speed tomographic particle image velocimetry (T-PIV) to reacting flows. This technique enables 4D spatio-temporal measurements of the fine-scale turbulent velocity field internal to a combustor, which is essential for understanding fluid/chemistry interactions.

2. We demonstrated the first application of 10 kHz repetition-rate CH_2O planar laser induced fluorescence (PLIF) using a diode pumped solid state laser, providing time resolved measurements of the fuel decomposition region.

3. We performed the first simultaneous T-PIV with PLIF, enabling quantification of 4D fluid/chemistry interaction.

4. We observed significant departures from the scalar structure associated with stretched pseudo-laminar premixed flame fronts as turbulence intensities were increased. Specifically, the distribution of the CH_2O molecule broadened to several times that of a laminar flame, demonstrating the effects of enhanced turbulent diffusivity within the instantaneous flame structure. However, the regions of high enthalpy release remained

1

thin and compact at all conditions tested, as indicated by the overlap of OH and CH_2O distributions.

5. We developed analytical techniques for pseudo-Lagrangian tracking of theoretical fluid particles that trace trajectories through the turbulent reacting flow. These particles enable the first experimental quantification of key metrics of the local fuel consumption rate.

6. We observed significant departures from the local fuel consumption rate expected of laminar flamelets, despite the regions of heat release remaining topologically similar to laminar flames. Specifically, local consumption rates increased proportionally to the local broadening of the CH_2O layers relative to a laminar flamelet, which is consistent with local turbulent diffusivity arguments. To our knowledge, this is the first experimental demonstration of increased local consumption rate due to turbulence enhanced diffusion, though this effect was hypothesized by Damköhler in 1940 [1]. It is noted that the persistence of the compact regions of intense energy release point towards improved modeling possibilities based on relatively small modifications to existing theories; the requirement is accurate modeling of the turbulence-enhanced rates in these regions and the volumes occupied by them.

A more detailed discussion of each of these accomplishments is provided below. Further information can be found in the publications arising from this project, which are detailed in Section 9.

2 Tomographic PIV in reacting flows

This work demonstrated the first tomographic PIV applied in reacting flows. Two T-PIV experimental campaigns were performed, the first in collaboration with Dr J. Frank and Dr. B. Coriton of Sandia National Laboratories, and the second with Dr. C. Carter of the Air Force Research Lab. The second campaign was supported by resources from Prof. T. Lee of the University of Illinois.

The objective of the first campaign was to assess the challenges and viability of the T-PIV technique for turbulent flames. Specifically, we needed to assess the effects of light steering through index of refraction gradients, seed density variations associated with fluid expansion, and background luminosity on tomographic reconstruction techniques. In this case, the T-PIV was combined with OH PLIF as a marker of the product gases. Measurements were performed at repetition rates from 10-16 kHz in a non-piloted lifted non-premixed flame, a piloted non-premixed flame, and a piloted premixed flame, all using dimethyl ether (DME) fuel. The second campaign targeted the highly turbulent premixed flames of interest to AFOSR, and also implemented CH_2O PLIF. The experimental configurations for each campaign are shown in Fig. 1, and the turbulent premixed jet flame configuration used for AFRL campaign is shown in Fig. 2. Test conditions for the AFRL campaign are given in Table 1

Each T-PIV system consisted of a diode pumped solid state Nd:YAG laser (Quantronix) and four high-speed CMOS cameras (Vision Research and Photron). Sub-micron particles (either alumina or titanium dioxide) having low Stokes numbers were used as flow tracers.
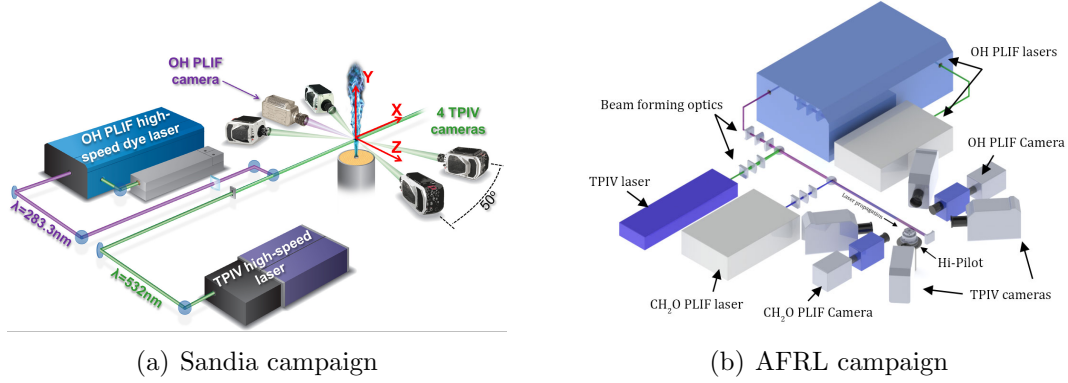
2

(a) Sandia campaign   (b) AFRL campaign

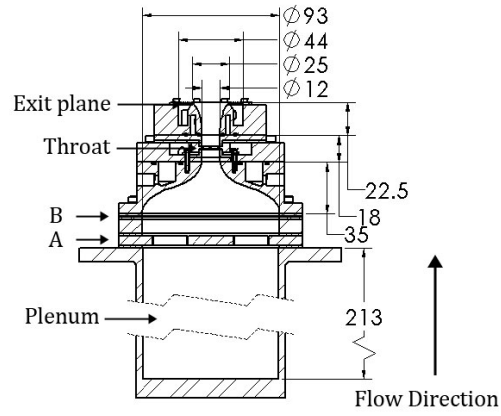**Figure 1** Laser diagnostics setups for Sandia and AFRL experimental campaigns.

Figure 2 Hi-Pilot burner configuration.

Table 1 Turbulence properties for each case based on hot wire anemometry, where U_{jet} is the bulk velocity, U_{cl} is the centerline velocity at the measurement location, $\dot{m}_p$ is the mass flow rate of the pilot, y_m is the measurement location, D_t is the burner throat diameter, u'_y is the root-mean-squared axial velocity fluctuations, Re_T is the turbulence Reynolds number, λ_k is the Kolmogorov length scale, Ka is the Karlovitz number, and Da is the Damköler number.

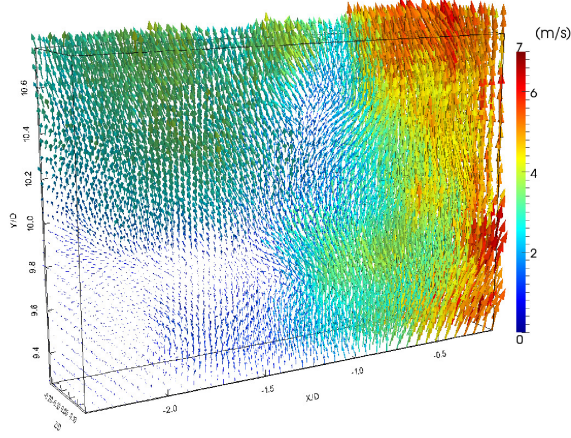| Case	U_{jet} (m/s)	$\dot{m}_p$ (g/s)	U_{cl} (m/s)	ϕ	y_m/D_t	Location	u'_y (m/s)	Re_T	$\lambda_k(\mu m)$	Ka	Da
1	1.9	0.008	6.8	0.85	1.6	Exit	0.40	87	236	5.0	40
						y_m	1.34	269	93	32.2	11
2	7.1	0.008	23.6	0.85	2.56	Exit	2.19	464	99	28.5	16
						y_m	5.50	2092	39	188.6	5.2
3	11.1	0.015	25.7	0.85	3.2	Exit	4.21	2794	54	97.9	12
						y_m	10.16	5738	27	396.8	4.1

3

Figure 3 Example T-PIV field. One in every 64 calculated vectors shown for clarity.

Camera calibration and registration was performed by using custom thin-film transparent dot targets. Velocity vector calculation was performed using commercial software (LaVision) and consisted of camera volume calibration, preprocessing of the particle images, camera self-calibration, reconstruction of the 3D particle field, determination of the local velocity vectors, and post-processing of the vector fields. A typical measured vector field is shown in Fig. 3. The field of view for the T-PIV was approximately 20 mm×20 mm×4 mm, with a resolution of approximately 0.5 mm and a 75% vector overlap.

The Sandia campaign was use to assess the basic capabilities of the T-PIV. In designing experiments for studying the temporal evolution of flow structures, it is important to evaluate the fidelity with which the measurements capture the dynamics of different fluid dynamic scales. While this has traditionally been done in an *ad hoc* manner, we derived several metrics to quantify how well the measurement temporal resolution captures the dynamics of the smallest spatially resolved scales, and whether the complete dynamics of a structure are captured in the measurement domain. The adequacy of the temporal resolution can be determined from the ratio of the inter-measurement time, Δt_m, and the turn-over time of the smallest resolved turbulent structures, $\tau(\lambda_m)$, viz. $C_e = \Delta t_m / \tau(\lambda_m)$.

The C_e parameter is analogous to the Courant-Friedrichs-Lewy (CFL) number employed in simulations and, according the Nyquist criterion, should be less than $1/2$ if the experiment is to resolve the dynamics of the smallest measured spatial scales. We showed that this parameter is related to turbulence properties as

$$C_e = \frac{\Delta t_m u'}{\lambda_m^{2/3} \delta^{1/3}} \tag{1}$$

where δ is the local integral scale.

We also defined a parameter D_e that describes whether the critical dimension of measurement domain, l_{FOV}, is sufficient to capture the turn-over time of a particular scale of structure, viz.

$$D_e(\lambda) = \frac{u'}{\bar{u}_y} \frac{l_{FOV}}{\lambda^{2/3} \delta^{1/3}} \tag{2}$$

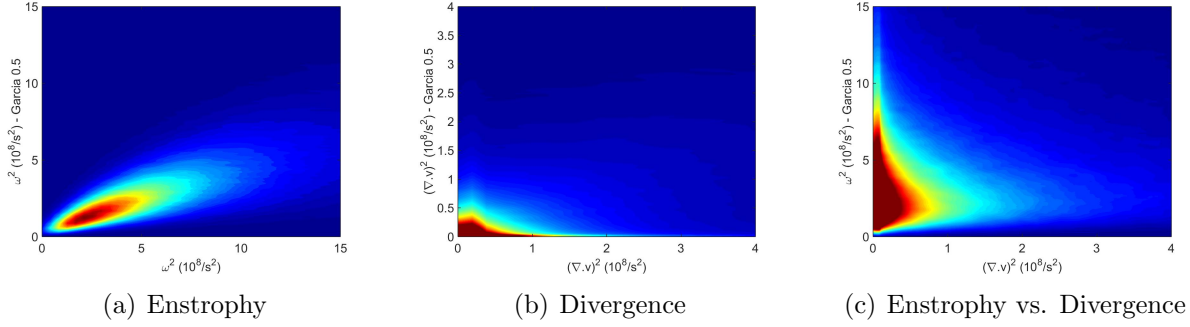In all cases studied, C_e was sufficiently low that all temporal dynamics of spatially-resolved

4

Figure 4 Effects of smoothing on velocity gradients. **a** Smoothed and unsmoothed enstrophy. **b** Smoothed and unsmoothed divergence. **c** Smoothed enstrophy and divergence. All smoothing is performed using a penalized least squares method with $s = 0.5$.

structures could be measured. However, the measurement domain was not sufficiently long to capture the full evolution of the largest scale structures (i.e. the slow moving dynamics), particularly for cases with high convective velocity. This limitation is hardware based; it is set by sensor resolution and data throughput.

Beam steering and background luminosity were assessed and not found to significantly affect the measurement accuracy. Additionally, we assessed the capability of T-PIV to measure gradient quantities, such as vorticity and strain rate. In principle, the complete velocity gradient tensor is available from TPIV measurements of the three-dimensional velocity field. In practice, the accurate measurement of velocity gradients presents a challenge because calculations of derivatives are sensitive to measurement noise and errors. A turbulent air jet was used to evaluate these effects, as the mass conservation condition in a constant density flow requires that the flow divergence is zero, $\nabla \cdot \vec{u} = 0$.

Three smoothing schemes were examined, a moving average (i.e. box), Gaussian, and penalized least squares filter kernel with various smoothing parameters [2]. All smoothing schemes followed similar trends, and only the results from the penalized least squares method with a smoothing parameter of $s = 0.5$ are discussed here.

Figure 4 shows a joint PDF of smoothed and unsmoothed enstrophy. While the smoothing reduced the calculated enstrophy, the smoothed and unsmoothed values remain highly correlated. This indicates that the measured enstrophy structures are spatially coherent. Conversely, the joint PDF of smoothed versus unsmoothed divergence shows essentially no correlation, as demonstrated in Figure 4b. This implies that smoothing maintains the structure of the enstrophy field while reducing the noise levels. The penalized least squared method with $s = 0.5$ was found to provide a good balance of preserving the enstrophy and reducing the divergence, and hence was used for all subsequent analysis.

Furthermore, the relation between noise and true velocity gradients was examined by plotting a joint PDF of enstrophy and squared divergence, given in Figure 4c. As shown, large values of divergence correspond to small enstrophy values, and vice versa, indicating that large velocity gradients tend to be more accurately measured than small gradients. Additional metrics and demonstrations of the T-PIV capabilities can be found in the associated publications.

3 High-speed CH$_2$O PLIF

CH$_2$O PLIF was performed as part of the AFRL measurement campaign, in order to detect the spatial-temporal behavior of the fuel breakdown regions, which correspond to reactant preheating. The CH$_2$O PLIF setup consisted of a frequency tripled Nd:YAG laser (EdgeWave) operating at 10 kHz, a high-speed CMOS camera (Photron) coupled to an image intensifier (LaVision), and a UV lens (Sodern). The pulse energy of the 355 nm laser at the measurement location after sheet formation was 1.6 mJ. A concave cylindrical mirror, coated for 280-355 nm, is used to retro-reflect both the OH and the CH$_2$O beams back through the probe volume, which effectively doubled the PLIF signals. The laser excited the A-X4$_0^1$ transition of formaldehyde in a bandwidth around 355 nm. To better concentrate pulse energy, the sheet height was set smaller than the TPIV at 7.5 mm. Fluorescence in the range of 370-480 nm was isolated using a Schott KV-389 filter.

The low fluorescence yield of the CH$_2$O and low pulse energy requires careful evaluation of the signal-to-noise ratio (SNR) and the conclusions that can be drawn from the measurements. Particular care was taken here to ensure that interpretation of the data was robust to the SNR and any image processing performed to aid in visualization. Typical recorded PLIF images from Case 3 (lowest SNR) are shown in Figure 5a, where red represents the OH PLIF (described below) and blue is the CH$_2$O PLIF. As seen qualitatively, there is substantially more noise in the CH$_2$O PLIF images than in the OH images. Despite this, there are discernible structures present in the CH$_2$O fields; there are regions of low CH$_2$O in the products (OH containing regions) where the CH$_2$O has been consumed and in the fresh reactants prior to OH formation.

Processing of the raw CH$_2$O images included binning, noise subtraction, and filtering. Identifying the CH$_2$O-containing regions was then done by thresholding the images. To ensure the data presented was independent of the image processing, this thresholding parameter was varied between 50% and 200% of the final value used in all data sets. No difference was found in the location of the identified CH$_2$O-containing regions across this range of thresholds. Hence, the qualitative identification of CH$_2$O containing regions was robust despite the relatively low SNR. The SNR was calculated based on the raw images (not the processed images) and found to range from 2.6-5.6 for the different cases. The CH$_2$O-containing region became broader with increasing turbulence intensity, resulting in lower concentrations and lower SNR with increasing turbulence.

Seeding particles contribute to background noise in the CH$_2$O PLIF measurements. Images therefore also were taken with no seed to ensure that all interpretation was robust. The data without seed typically had a SNR approximately 20-50% higher than data with seed, but no qualitative change was observed in flame structure as a result of this higher SNR.

4 Combined T-PIV/OH PLIF/CH$_2$O PLIF

The complete set of scalar measurements consisted also included OH PLIF to mark regions of hot products. Furthermore, the spatial overlap between instantaneous OH and CH$_2$O fields describes the topology of the regions containing high enthalpy release. The OH PLIF system used the second harmonic output of a Nd:YAG laser (EdgeWave) operating at 10 kHz to
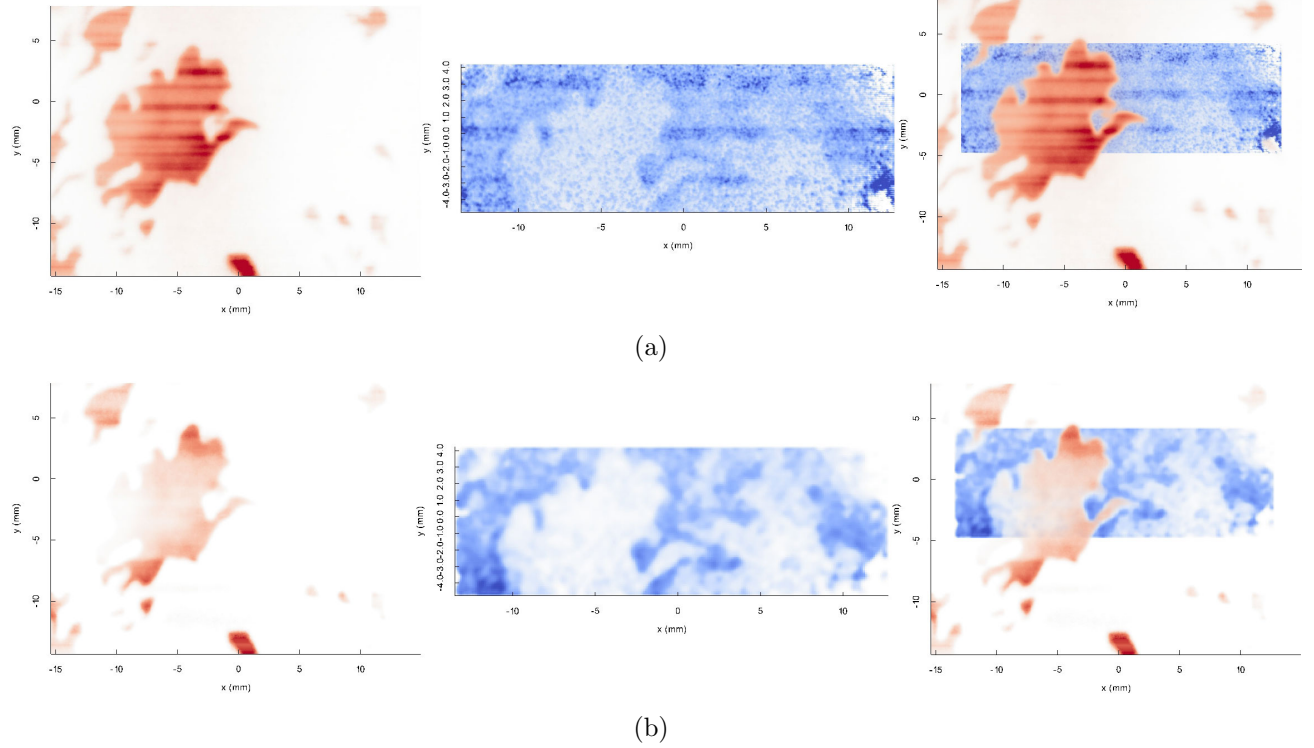
(a)

(b)

Figure 5 Example of OH PLIF (red), CH$_2$O PLIF (blue), and overlap from Case 3. **a** Typical raw images. **b** Processed images.

pump a dye laser (Sirah) with Rhodamine 6G dye solution, and a high-speed CMOS camera (Photron) coupled to an image intensifier (LaVision). The frequency doubled dye laser output (0.2 mJ/pulse) was tuned to excite the Q$_1$(7) line of the A-X ($v' = 1$, $v''=0$) band of OH at approximately 283.2 nm. Fluorescence in the range of 310 nm was isolated using a bandpass filter, and collected into the intensified camera using a fast UV lens (Sodern). The two PLIF pulses were separated by approximately 700 ns, and occurred between the TPIV pulses for each measurement. The position of the PLIF sheets concided with the center of the TPIV beam. A 3rd order polynomial warping algorithm was used to match the target images of the PLIF and TPIV, where the PLIF target image was the thin-film transparency on the z = 0.0 mm plane.

5 Departure of scalar structure from laminar flamelets

The simultaneous PLIF measurements, in combination witht Mie scattering associated with the T-PIV allow evaluation of the scalar structure and topology of the flame. Sample images showing the superposition of the OH and CH$_2$O PLIF for Cases 1-3 are shown in Figure 6. Figure 6a shows a very clear laminar-like structure to the CH$_2$O layer at the low turbulence intensities of Case 1. The transition from low-to-high OH signal is sharp and the OH and CH$_2$O do not broadly overlap, indicating thin heat release regions. This is consistent with the flame being in the laminar flamelet regime.

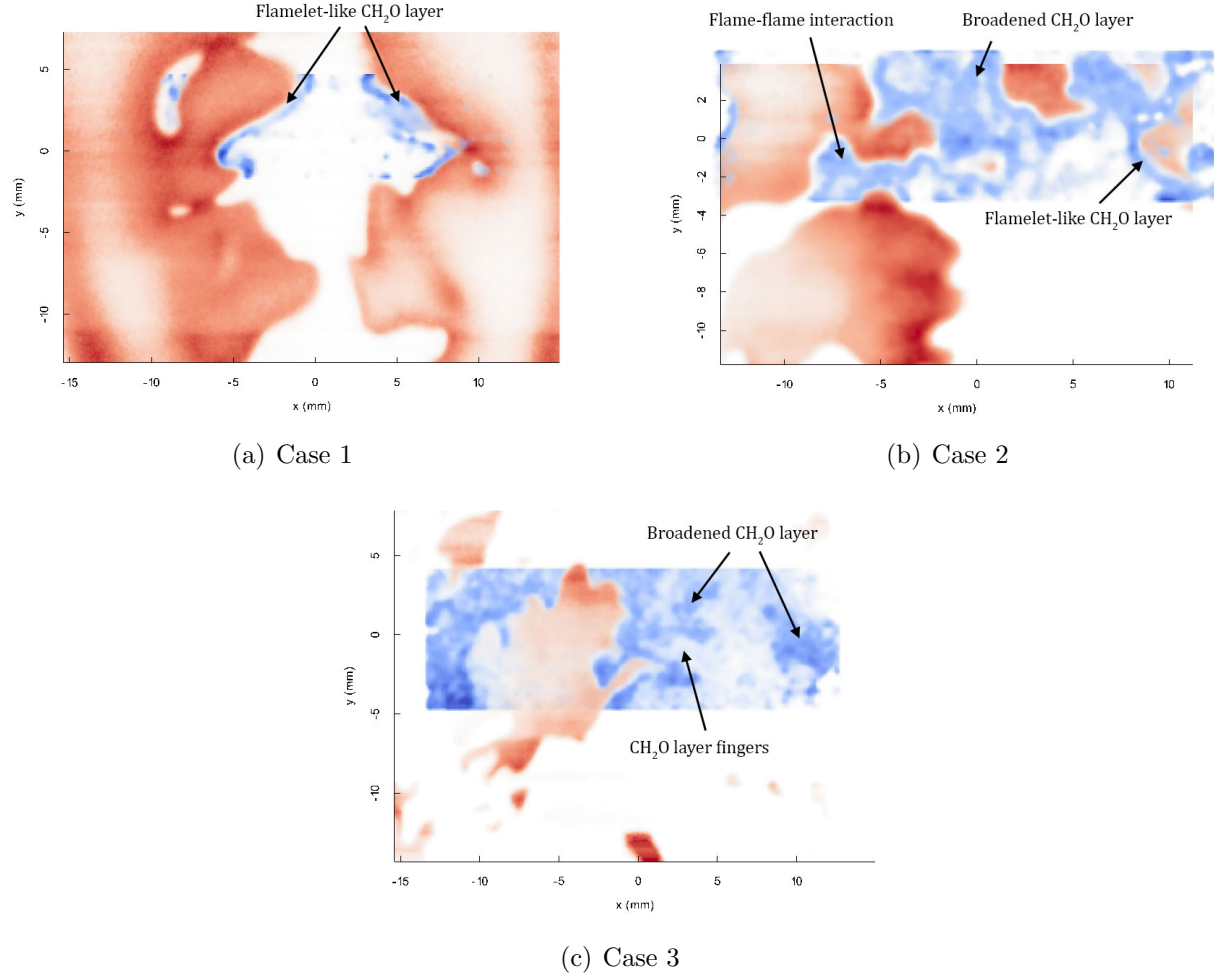The images in Figure 6b of Case 2 shows examples of CH$_2$O layer merging, the formation

(a) Case 1

(b) Case 2

(c) Case 3

Figure 6 Typical OH PLIF and CH$_2$O PLIF images for Cases 1-3. Color scale as per Figure 5.

of detached reactant pockets through flame-flame interaction, as well as examples of both flamelet-like and broadened CH$_2$O regions. Similar to Case 1, the OH gradients are sharp and the overlap between OH and CH$_2$O is thin. Hence, Case 2 appears to be a transitional state between the laminar flamelet and thickened preheat zone/thin reaction zones regimes.

As the turbulence intensity increases to Case 3 in Figure 6c, CH$_2$O appears more broadly distributed. There is little correlation between the topology of the OH layer and the upstream (reactant side) of the CH$_2$O region, which has numerous turbulence-induced structures, e.g. long CH$_2$O 'fingers' protruding into the reactants. However, Case 3 continues to show sharp OH transitions and low overlap between CH$_2$O and OH. While there is significant local extinction in both cases as indicated by the discontinuities in the OH layer, there is no evidence of broadly distributed heat release. This flame therefore is characterized by broadened preheat zones and thin (but broken) reaction zones.

When investigating flame structure and topology from 2D measurements, it is important to account for the 3D nature of the flame. For example, significant out-of-plane orientation can result in perceived thickening of scalar layers in planar images. Three dimensional measurements of flame structure have been made by tomography [3, 4, 5], multi-plane measurements [6], and scanning mirror measurements [7]. However, each of these has some
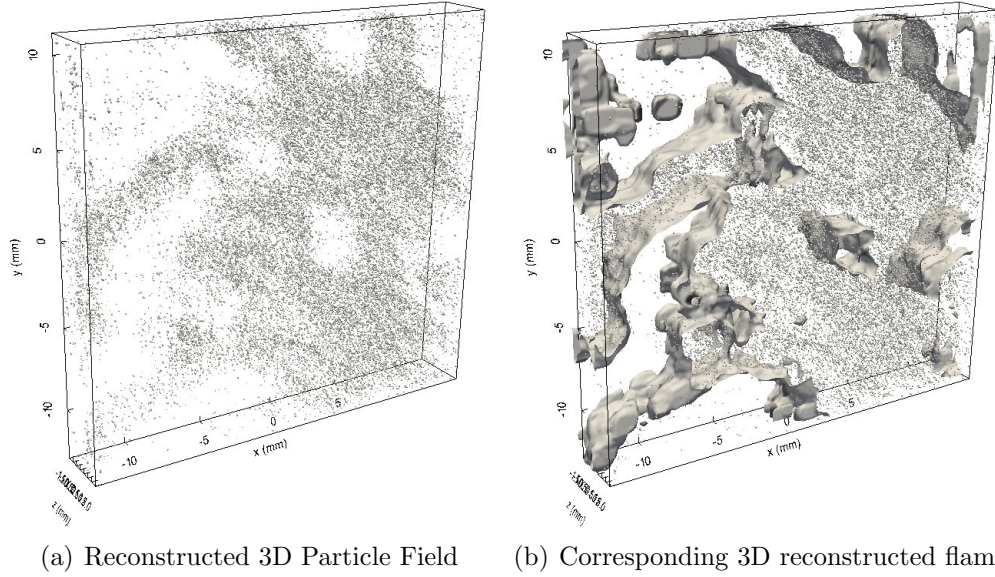
(a) Reconstructed 3D Particle Field   (b) Corresponding 3D reconstructed flame

Figure 7 Mie scattering based flame detection example from Case 2.

drawbacks for the current application. Tomography requires several simultaneous views to reconstruct the 3D field from 2D projections. High resolution requires a large number of views, which was not optically viable in this experiment. Furthermore, accurate reconstruction requires quantitative scalar signals from each of the views, which is difficult to achieve due to e.g. quenching and signal self-absorption. Multi-plane measurements also require additional detectors and lasers, which was not possible. Furthermore, such measurements provide limited 3D resolution, generally utilizing only two planes for practical reasons. The limitation in number of planes is alleviated in scanning mirror measurements, but the data are no longer instantaneous. Extremely high scanning and measurement rates would be required to effectively freeze the flows studied here, which was not experimentally viable.

Instead, the Mie scattering tomography was used to gain insight into the 3D flame geometry. Mapping the 2D topology of turbulent premixed flames in the laminar flamelet regime using Mie scattering previously has been done by utilizing the drop in particle number density between reactants and products [8, 9]. For seed that does not survive the flame, such as olive oil, the density drop is sharp near a particular isotherm where the seed evaporates. For solid particles that survive the flame, such as the titanium dioxide used here, the decrease in particle seed density is a result of the decrease in gas density as the reactants expand to the products.

Here, this technique was extended to 3D by utilizing the Mie scattering volumes that are tomographically reconstructed as part of the TPIV processing. The particular challenge for tomography is that the volumetric number density of seed particles is lower than for planar PIV applications, so as to avoid excessive seed particle overlap in the different viewing angles. This has the potential to add noise and reduce resolution in the topology measurements. Nevertheless, a sharp decrease in seed particle density was observed in most cases, as was shown in Figure 7a for Case 2.

To reconstruct the corresponding 3D topology, the overall volume first binned, filtered, converted to binary, and then had small gaps filled using a 3D filling algorithm. The 3D

9

flame surface thus determined from the Mie scattering field in Figure 7a is shown in Figure 7b.

Properly selecting the threshold value is critical for accurately defining the 3D flame topology. While the topology of laminar flamelets (e.g. Case 1) is relatively simple to define since density gradients are sharp and scalar isosurfaces are parallel, the distributed CH_2O regions observed in Cases 2 and 3 indicate reduced density gradients and non-parallel isosurfaces. However, the fact that OH gradients remain sharp and CH_2O/OH overlap regions remain thin for all cases allows extraction of a topological surface from the Mie scattering that corresponds to the generation of OH. This surface represents the reactant side of the thin heat release layers.

To determine the optimal threshold value for identifying this surface, 3D flame topologies on the $z = 0$ plane were compared to OH PLIF images at various threshold levels. The OH images were binned to match the resolution of the 3D flame, binarized to distinguish product from reactants, and then compared to the 3D reconstruction. To make the comparison between the OH and reconstructed flame, the 2D projection of the 3D flame topology and the curve representing the OH were each represented as parametric space curves, $\zeta_{3D}(\xi_{3D}) = x_{f,3D}(\xi_{3D})\hat{i} + y_{f,3D}(\xi_{3D})\hat{j}$ and $\zeta_{OH}(\xi_{OH}) = x_{f,OH}(\xi_{OH})\hat{i} + y_{f,OH}(\xi_{OH})\hat{j}$. As ξ_i increases, $x_{f,i}$ and $y_{f,i}$ trace out the different flame curves. For each value of ξ_{3D}, the minimum distance between ζ_{3D} and ζ_{OH} was calculated. This process was repeated using various threshold levels for the 3D reconstructions, and the final 3D flame was chosen based on the minimum mean difference between the two curves across all images.

Using the final selected threshold value for the 3D reconstruction, statistics on minimum distance between ζ_{3D} and ζ_{OH} was determined, which are presented in Figure 8 for Cases 1-3. As the ability to reconstruct the 3D flame depends on both the flow density gradient across the flame and the seeding density, the accuracy of the reconstruction is highly case dependent. Case 3 had the lowest accuracy of the three reconstructions through a combination of relatively low seeding density and shallow density gradients.
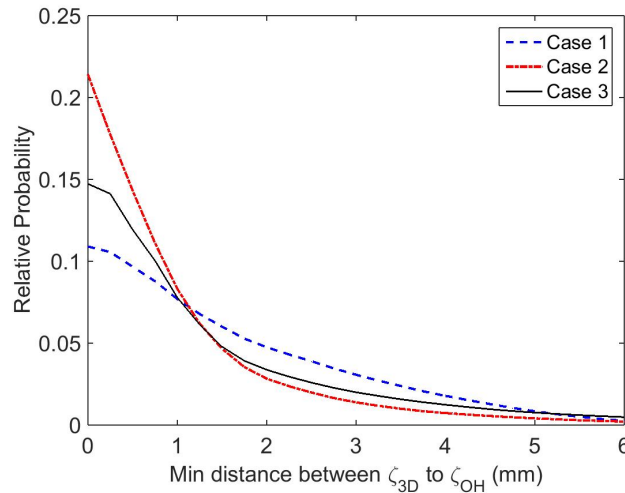

Figure 8 Minimum distance between ζ_{3D} and ζ_{OH} for Cases 1-3

Figure 9 shows an example cross-section of the 3D topology superimposed on the OH PLIF plane for Cases 1-3. As can be seen, the 3D topology is capable of capturing the general
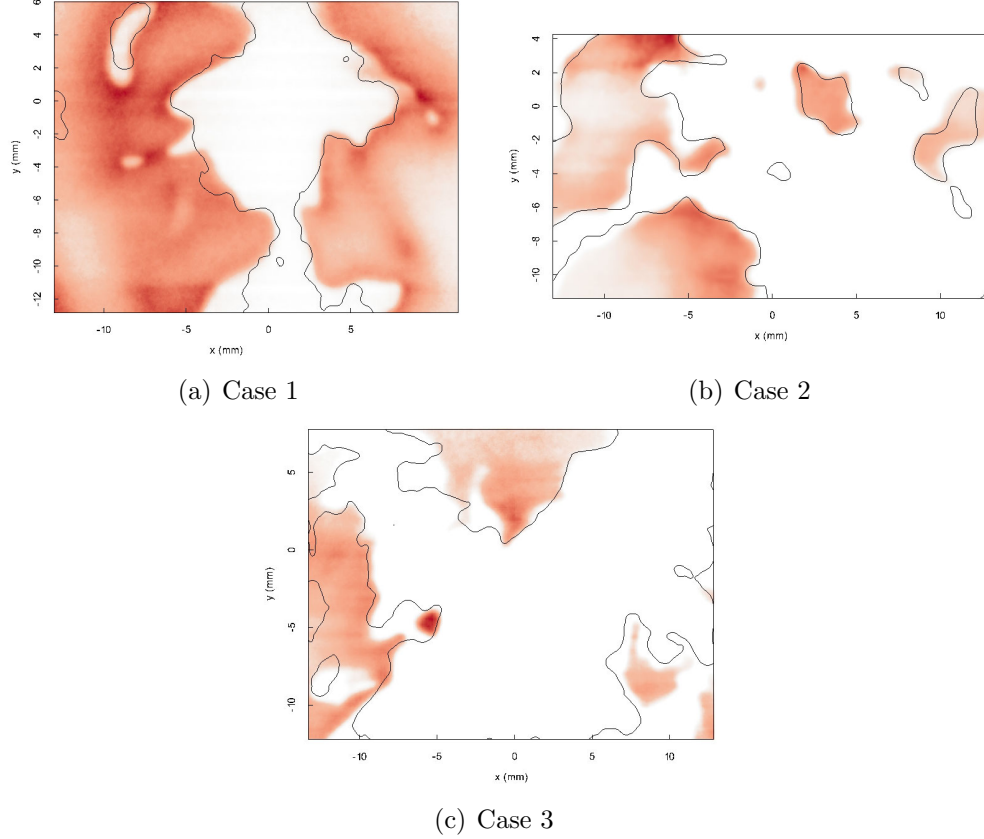
10

(a) Case 1

(b) Case 2

(c) Case 3

Figure 9 Typical 3D reconstructed flame at the z = 0 mm plane (solid line) with corresponding OH PLIF for Cases 1-3.

shapes and structure of most OH layers. However, because the 3D reconstruction is based on the distribution of particles, the reconstruction can deviate from the OH PLIF for two main reasons. Firstly, natural inhomogeneity in the seeding flow or laser illumination can result in local volumes of reactants with low seed. This tends to result in regions with rather smooth deviation between the OH and 3D flame, as seen towards the bottom of Fig. 9a. Secondly, the binning and smoothing of the particle field reduces the effective spatial resolution of the measurements, resulting in the 3D reconstruction occasionally missing fine-scale features such as that around (-5 ,-3 mm) of Fig. 9a. Despite these issues ,the 3D reconstructed can be used to deduce the general 3D flame shape and orientation. Further details regarding the impact of non-flamelet structures on reaction rate are provided below.

6 Lagrangian tracking algorithms

The availability of 3D time resolved velocity fields allows for the tracking of theoretical Lagrangian particles (TLP) through the flow field. TLPs are massless and non-diffusive 'particles' that are computationally placed in the measured velocity fields and move with the flow. The TLPs act as passive flow tracers, allowing calculation of various properties along Lagrangian trajectories as the particles interact with the flame scalar structure.

The use of TLPs to study the Lagrangian behavior of turbulence is well established for

11

DNS data sets, but has not been widely employed for experimental measurements due to the lack of time-resolved 3D velocity fields [10]. At a time t^*, the position of particle j having an initial position of $\vec{X}_{j,0}$ at time $t_{j,0}$ is $\vec{X}_j \mid_{t^*} = \vec{X}_j \left(\vec{X}_{j,0}, t_{j,0} \mid t^* \right)$. The evolution of the particle position is governed by

$$\left. \frac{d\tilde{X}_j}{dt} \right|_{t^*} = \left. \vec{U}_j \right|_{t^*} \tag{3}$$

where $\left. \vec{U}_j \right|_{t^*} = \vec{u} \left(\vec{X}_j \mid_{t^*}, t^* \right)$, $\vec{U}$ is the Lagrangian velocity and $\vec{u}$ is the Eulerian velocity. This formulation essentially treats the TLPs as passive, massless, non-diffusive flow tracers that follow the velocity field.

Accurately solving Eq. 3 is not trivial, particularly for finite resolution experimental data that exhibits noise. Four interpolated time steps were used between each measured time step, and four-dimensional (nominally fourth-order) cubic-spline interpolation (in both space and time) was used to calculate the velocity at the instantaneous particle locations [11]. TLPs were placed into the measured velocity field with a density corresponding to the inter-vector spacing from the TPIV. As particles left the measurement volume, new particles were inserted in open locations, thereby keeping the total number of particles constant.

An issue that arises with TLP tracking through experimental data is that erroneous local instantaneous vectors can cause considerable error in the evolution of an individual particle; once error is induced in the particle position, this error grows exponentially with time. While erroneous vectors could be reduced through increased outlier detection or smoothing, these methods also affect the other non-erroneous vectors. It therefore was decided to track ensembles of particles together, instead of individual particles.

The idea is shown conceptually in Figure 10 for a 2D configuration. An ensemble of particles in the reactants convect in the flow direction. The particle ensemble centroid (PEC) is taken as the characteristic position of the ensemble. Individual outlier particles caused by measurement noise can be identified based on the mean velocity in the ensemble, and eliminated from the centroid calculation. After each time step, a new ensemble of particles is identified around the centroid of the previous ensemble, and used for the subsequent time step. For all analysis here, the chosen ensemble size was selected to be equal to the interrogation volume size, and thus contained about 125 individual vectors in a ca. 0.6 mm sided cube due to the interrogation volume overlap.
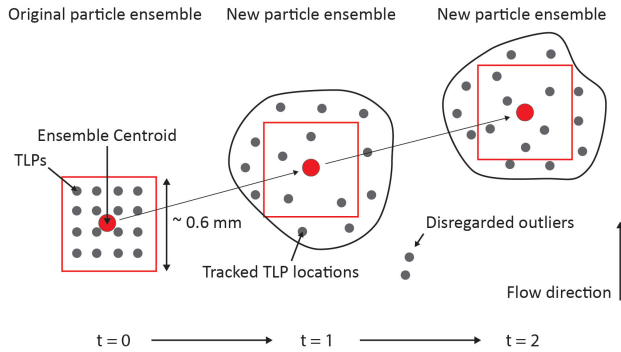

Figure 10 Concept of Lagrangian particle ensemble (LPE) tracking
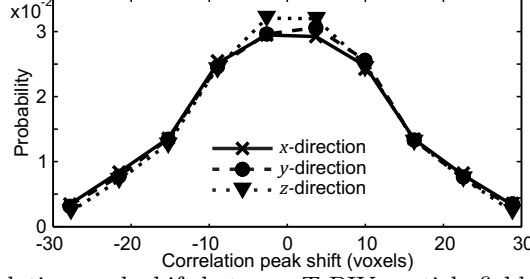
12

Figure 11 PDFs of cross-correlation-peak shift between T-PIV particle fields around Lagrangian particles at subsequent times.

Uncertainty in the PEC tracking over single frames was empirically assessed by comparing the directly-measured T-PIV particle fields around subsequent locations of a given PEC. If the PEC was tracked correctly, the T-PIV particle fields around the PEC should be similar. Cross-correlations therefore were performed between the particle fields in $32 \times 32 \times 32$ voxel regions around subsequent location of 200,000 PECs. Figure 11 shows the PDFs of the correlation peak location in pixels for each coordinate direction. As can be seen, the most probable correlation-peak was at zero-shift. The mean magnitude of the correlation peak shift in each direction was approximately 10 voxels, or $150\,\mu$m. The PECs therefore appear to be well tracked through time.

Tracking errors are cumulative when calculated across multiple time steps. In order to quantify these errors, PEC were tracked in a variety of test flow fields. The test flow fields were designed to produce similar cumulative errors in PEC tracking as would be anticipated in the experimental flows. To that end, the fields had a constant shear rate of $S = \partial u_x / \partial y$, superimposed on a uniform convective velocity ($\bar{u}_y$). Different values of S were selected to represent different strengths of turbulence, and the convective velocity was set to be approximately that of Case 2. Hence, the velocity fields were given by $\vec{u} = (Sy, \bar{u}_y, 0)$. From this, the ideal position ($\vec{\chi}$) of a particle at some time t^*, that started at an initial position $\vec{X}_{j,0} = (x_0, y_0, 0)$ is

$$\vec{\chi}_j \mid_{t^*} = \left(\frac{S(\bar{u}_y t + y_0)^2}{2\bar{u}_y} + \left[x_0 - \frac{Sy_0^2}{2\bar{u}_y} \right], \bar{u}_y t + y_0, 0 \right) \tag{4}$$

The exact particle positions were compared to those calculated using the PEC ensemble tracking algorithm. The algorithm was applied to the test vector fields sampled at 150 μm vector spacing and 0.1 ms between tracking time steps, which was the same as the experiment. Moreover, to account for the effects of noise in the measurements, $\pm 0.05\bar{u}_y$ of normally distributed white noise was added to the test flow field.

An example of the exact and tracked particle positions is shown in Figure 12 for $S = 10^3$ s^{-1} over 6 time steps, after which a portion of the particle ensemble left the domain. To quantify the error over time, the difference between tracked and exact positions ($\left| \vec{\chi}_j \mid_{t^*} - \vec{X}_j \mid_{t^*} \right|$) were measured at each time step and each value of S. This tracking error was calculated over a range of S values, shown in Figure 13 as a function of tracking time. Tracking errors typically were less than about 1 mm, even for flow exposed to the highest velocity gradients for long durations.

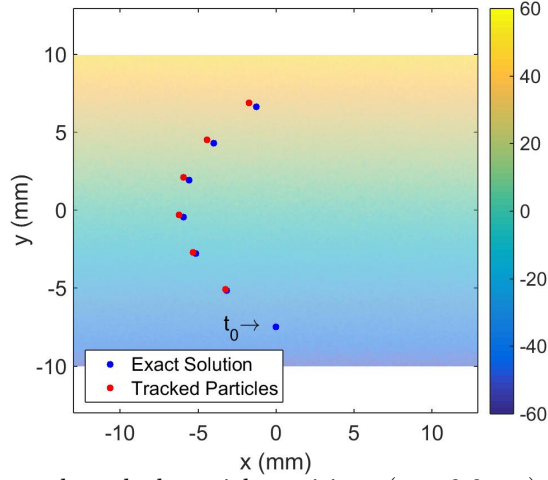The tracking validated algorithms described above are essential for quantifying the local

Figure 12 Example of exact and tracked particle positions ($z = 0.0$ cm) for $S = 10^3$ s^{-1}. Contoured by x-velocity in m/s. Only centroid of tracked control mass is shown for clarity
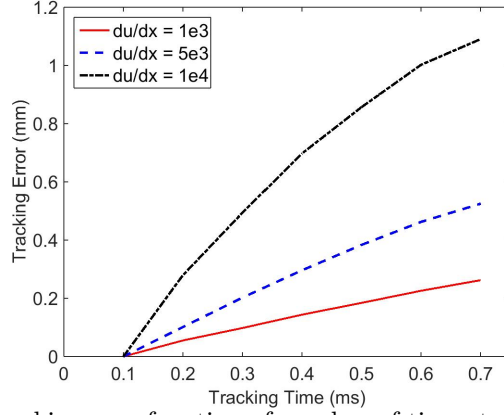

Figure 13 Error in particle tracking as a function of number of time steps

reaction rate of turbulent premixed flames, as described below.

7 Local reaction rate

Two metrics were proposed to characterize the local reaction rate. The first is based on the time required for a fluid element to traverse the local flame structure. The second simultaneously utilizes this residence time and the local flame thickness to determine a flame speed metric.

The time required for the flame to traverse its thickness is a fundamental property characterizing the reaction rate of a premixed flame. For example, a planar laminar premixed flame propagates the distance between the location of peak heat release and the leading edge of the preheat zone in a time $\tau_c \propto \delta_l/s_l \propto \rho_u/\dot{m}_r$, where ρ_u is the density of the unburnt gas and $\dot{m}_r$ is the volumetric mass consumption rate of reactants. Equivalently, this first metric of reaction rate τ_c can be viewed as the time required for an element of fluid to traverse from the leading edge of the preheat layer to the heat release layer, i.e. the residence time of the

14

fluid element within the flame.

However, some ambiguity in interpreting τ_c can arise due to variations in the local flame thickness (δ_f) relative to δ_l; flames with uniform reaction rate would have $\tau_c \propto \delta_f$. Thus, the second metric relating to flame speed can be defined as $S = \delta_f/\tau_c$, where δ_f is the local thickness of the flame segment through which the fluid element defining τ_c traverses.

To measure τ_c, the leading edge of the flame and heat release region are taken to coincide with the reactant side of the CH_2O and the location of rapid OH production, respectively. Calculation of τ_c requires tracking of fluid elements from the edge of the CH_2O layer to the edge of the OH layer, as shown conceptually in Fig. 14 for a 2D configuration. Definition of the initial position of a fluid element in the $z = 0$ plane can be made directly based on the CH_2O PLIF. However, the 3D nature of the turbulent flow results in fluid elements that were initially defined at $z = 0$ convecting in the z-direction during their τ_c. Hence, calculation of τ_c and S require both flow tracking and identification of the OH gradient (heat release) region in 3D.
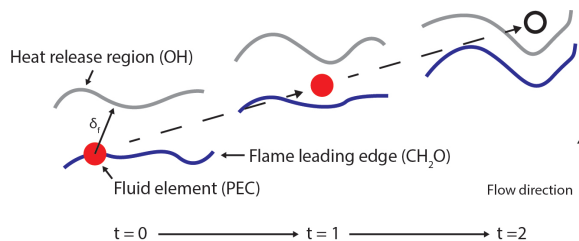

Figure 14 Concept of residence time measurement.

To determine the terms necessary for the reaction rate metrics, the leading edge of the flame first was identified by the CH_2O PLIF. A PEC then was placed on the nearest point in the TPIV grid (maximum distance between leading edge point and velocity vector was 0.0385 mm, which was insignificant to the calculation), and tracked using the algorithm described above, until it crossed the 3D surface associated with the OH PLIF.

The uncertainties associated with the overall calculation were tested using the same 1D laminar flame simulation used to determine s_l and δ_l. The upstream point on the flame from which a PEC was tracked was taken to be the location of the maximum CH_2O gradient, and the downstream point was taken as the location of maximum OH gradient. These should correspond well to experimental leading edge and measured 3D flame surface, respectively. A 3D simulation volume then was created in which the velocity field followed $\vec{u} = (u_x(x), 0, 0)$, where $u_x(x)$ is the velocity profile calculated from the laminar flame simulation. The domain was discretized onto an analogous grid to the TPIV, PECs were placed on the flame leading edge, and the PECs were tracked forward in time using a temporal discretization equal to experimental until they crossed the flame trailing edge. Linear interpolation between the PEC positions before and after they crossed the trailing edge was used to compute the residence time.

Monte Carlo-type simulations were performed to encompass a range of uncertainties expected to arise in the experimental cases; Gaussian noise with standard deviations of 0.5 mm, 0.25 mm, and $0.2\bar{u}_x$ were added to the positions of the OH edge, CH_2O edge, and velocity field respectively. The effect of the pilot on the results was considered negligible as the ratio of mass flow rates were ca. 125-500. Moreover, the effect PEC size on tracking
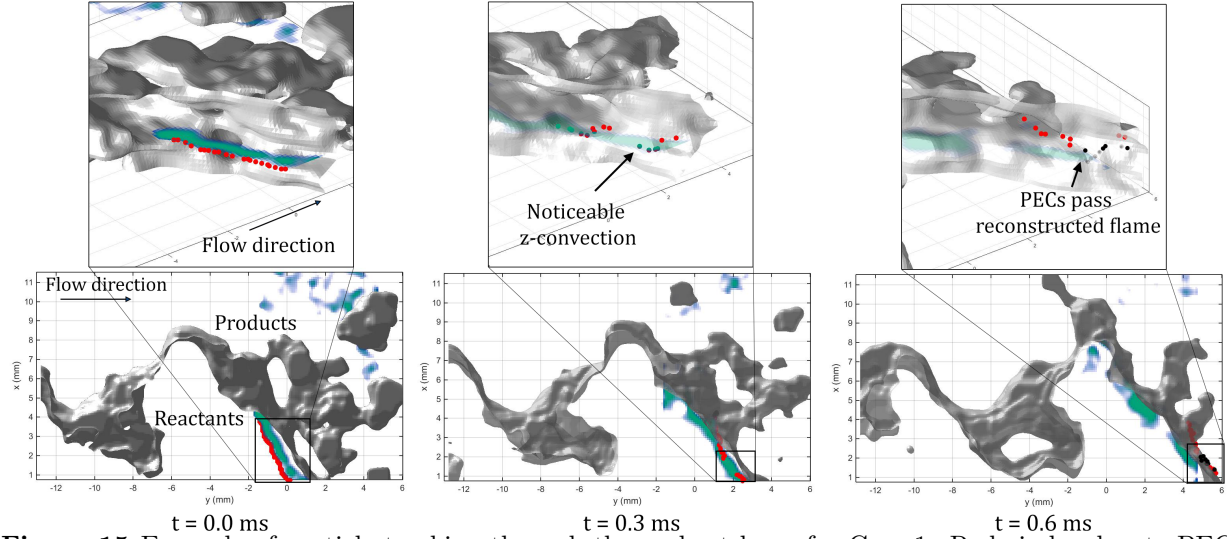
15

Figure 15 Example of particle tracking through the preheat layer for Case 1. Red circles denote PECs, black circles denotes PECs that have passed the flame surface, green contours is the extent of the CH_2O layer, and grey isosurface is the Mie scattering surface. Top and bottom images correspond to the same time steps. One in three particles shown for clarity

accuracy was also investigated by comparing the τ_c of a PEC with a single TLP, showing less than 1% change in τ_c. The uncertainty in τ_c was most predominantly driven by errors in flame position, with velocity errors contributing negligibly. The most probable τ_c for the simulated flame with input parameters best matching the anticipated errors in Case 1 was $\tau_{c,0} = 0.54$ ms. This represents theoretical values for a laminar flame against which the experimental results can be evaluated.

This residence time algorithm was applied to the two flames studied. An example of this tracking for Case 1 is shown in Fig. 15. The leading edge of the CH_2O (green layer) was first identified. PECs (red dots) were then placed along this 2D contour, and tracked forward in time until they crossed the Mie scattering-based flame (gray surface), after which they were no longer tracked (black dots). At each step, the minimum distance between the PEC and Mie scattering surface was determined, $d_{fi}(t - t_{0i})$, where i designates the PEC and t_{0i} is the time at which the PEC was at the leading edge of the CH_2O region. Hence, $d_{fi}(0) = d_{fi,0}$ is the initial distance from the leading edge of the CH_2O layer to the Mie scattering surface, which is a metric of the local flame thickness (i.e. $d_{fi,0} = \delta_f$).

Figure 16a presents d_{fi} versus $t - t_{0i}$ for a few typical PEC tracks for each case, as well as for the simulated laminar flame. Characteristic values of $d_{fi,0}$ were higher for Case 2 than for Case 1, which is a result of the CH_2O layer broadening observed in Fig. 6. However, despite the greater initial distance, the PECs for Case 2 crossed $d_f = 0$ in less time than those for Case 1; τ_{ci} for Case 2 is less than Case 1. Figure 16b shows the τ_c PDFs, which confirms the statistical reduction in residence time for Case 2. This demonstrates a significantly increased local reaction rate for Case 2 relative to Case 1. The most probable residence time of Case $1(\tau_{c,1} = 0.47$ ms) is also similar to the simulated flame ($\tau_{c,0} = 0.54$ ms).
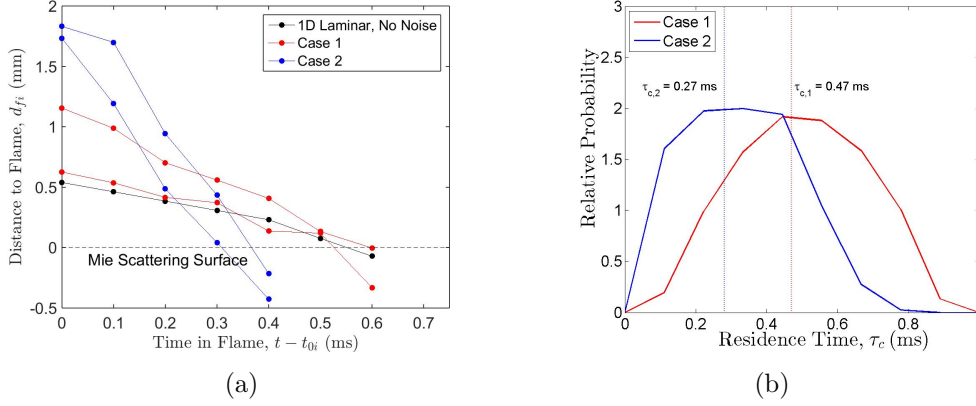
16

Figure 16 a Distance to flame for characteristic tracked particles. **b** PDF of residence time for simulated and studied flames.

If reaction rate was independent of the flame thickness, then $\tau_{ci} \propto d_{fi,0}$, and the speed metric, $S_i = d_{fi,0}/\tau_{ci}$, would be constant for each case. Figure 17 shows the joint PDF of S_i/s_l and $d_{fi,0}/\delta_l$ for each case (ca. 15,000 data points for each case), which clearly shows that S increases with the local flame thickness, indicating an increase in reaction rate with flame thickness. The bands in the joint PDFs are due to the spatial discretization of the Mie scattering flame surface, but do not affect interpretation of the results.
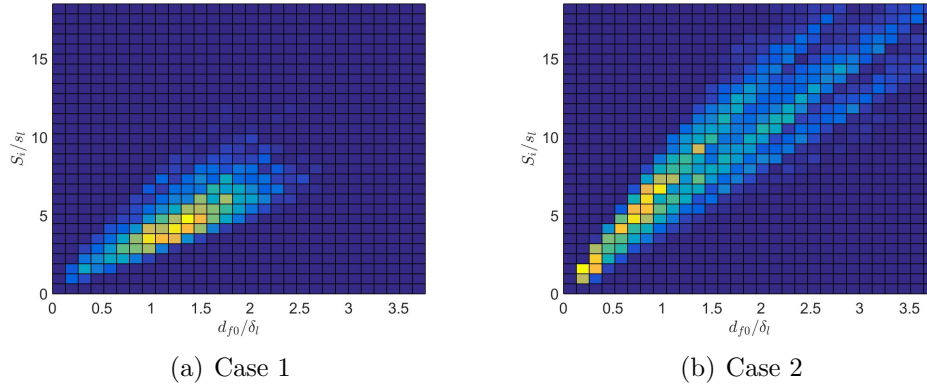

(a) Case 1   (b) Case 2

Figure 17 Joint PDF of S versus initial minimum distance to flame

The results demonstrate a linear correlation between between flame propagation rate and flame broadening, which is attributed to the increase in turbulent diffusivity. Flamelet theory indicates that

$$\frac{S}{s_l} \propto \left(\frac{\alpha_T + \alpha}{\alpha} \right)^{1/2} \tag{5}$$

$$\frac{d_{f0}}{\delta_l} \propto \frac{(D_T + D)/S}{D/s_l} \propto \left(\frac{\alpha_T + \alpha}{\alpha} \right)^{1/2} \tag{6}$$

where α and D are the thermal and molecular diffusivity, respectively, subscript T indicates a turbulent diffusivity, and $\alpha \propto D$. Hence, the trends observed here are consistent with

17

theory. To our knowledge, this is the first experimental demonstration of this relationship in a turbulent flame.

8   Future Work

Through this program, we have identified a critical aspect of turbulent combustion that must be accurately modeled for predictive simulations, namely the increased reaction rate per unit area of flame surface as the turbulence intensity is increased. This observation contributes to the currently emerging picture of turbulent combustion, in which the details of the turbulent field internal to the instantaneous flame scalar field must be understood. Future work should therefore should explain the coupled evolution of turbulence, combustion scalars, and reaction rate, in order to derive physics-based models.

Specifically, research should be undertaken that explicitly measures the evolution of turbulence through the flame, in combination with sufficient scalar data to characterize the fuel decomposition/preheat region and the regions of high enthalpy release. This work can take advantage of recent developments in 'shake-the-box' particle tracking and filtered Rayleigh scattering. Furthermore, the experiments should closely interface with scientists performing direct numerical simulations (DNS), to bridge the divide between realistic systems and the true physics (experiments), and the complete information on the thermo-chemical-fluid state available from the DNS.

9   Publications

Journal Articles (Published or Accepted):

1. J. R. Osborne, S. A. Ramji, C. D. Carter, A. M. Steinberg, Relationship between local reaction rate and flame structure in turbulent premixed flames from simultaneous 10 kHz TPIV, OH PLIF, and CH2O PLIF, *Proceedings of the Combustion Institute*, Accepted (2016)

2. J. R. Osborne, S. A. Ramji, C. D. Carter, S. Peltier, S. Hammack, T. Lee, A. M. Steinberg, Simultaneous 10 kHz T-PIV, OH PLIF, and CH2O PLIF measurements of turbulent premixed flame structure and dynamics, *Experiments in Fluids*, 57:65 (2016)

3. A. M. Steinberg, B. Coriton, J. H. Frank, Influence of combustion on principal strain-rate transport in turbulent premixed flames, *Proceedings of the Combustion Institute*, 35:1287-94 (2015)

4. B. Coriton, A. M. Steinberg, J. H. Frank, High-Speed Tomographic PIV and OH PLIF Measurements in Turbulent Reactive Flows, *Experiments in Fluids*, 55:1743-62 (2014)

*Two further journal articles currently are in preparation based on this work. Conference

Papers/Presentations (Published or Accepted):

1. J. R. Osborne, C. D. Carter, A. M. Steinberg, Particle dynamics through turbulent premixed flames using 10 kHz TPIV, OH PLIF, and CH2O PLIF, 24th International congress on Theoretical and Applied Mechanics (Accepted), Montreal QC (2016)

2. J. R. Osborne, S. A. Ramji, C. D. Carter, A. M. Steinberg, Relationship between local reaction rate and flame structure in turbulent premixed flames from simultaneous 10 kHz TPIV, OH PLIF, and CH2O PLIF, 36th International Symposium on Combustion (Accepted), Seoul South Korea (2016)

3. J. R. Osborne, C. D. Carter, A. M. Steinberg, Reaction rates in turbulent premixed flames measured from simultaneous 10 kHz TPIV, OH PLIF, and CH2O PLIF, Combustion Institute Canadian Section Meeting, Waterloo ON (2016)

4. J. R. Osborne, S. A. Ramji, C. D. Carter, S. Peltier, S. Hammack, T. Lee, A. M. Steinberg, Measurement of local flame speeds in the thickened flamelet regime using simultaneous 10 kHz TPIV and OH/CH2O PLIF, 51st AIAA Joint Propulsion Conference, AIAA-2015-4087, Orlando FL (2015)

5. J. R. Osborne, C. D. Carter, A. M. Steinberg, Reaction rate during flame-flame interactions in highly turbulent premixed jet flames measured using high-speed and simultaneous T-PIV and OH/CH2O-PLIF, CASI Aeronautics Conference, Montreal QC, 2015

6. S. A. Ramji, J. R. Osborne, C. D. Carter, A. M. Steinberg, Measurement of local flame consumption speeds in highly turbulent premixed flames using high-speed T-PIV and OH/CH2O PLIF, Comubstion Institute Canadian Section Meeting, Saskatoon SK (2015)

7. J. R. Osborne, C. D. Carter, S. Peltier, S. Hammack, T. Lee, A. M. Steinberg, Simultaneous high-repetition-rate tomographic PIV and OH/CH2O-PLIF in premixed flames across regimes., Comubstion Institute Canadian Section Meeting, Saskatoon SK (2015)

8. S. A. Ramji, A. M. Steinberg, B. R. Coriton, J. H. Frank, Evaluation of Lagrangian particle tracking algorithms for quantitative analysis of 4D experimental data, Combustion Institute Canadian Section Meeting, Windsor ON (2014)

9. A. M. Steinberg, B. R. Coriton, J. H. Frank Influence of combustion on principal strain-rate transport in turbulent premixed flames, Combustion Institute Canadian Section Meeting, Windsor ON (2014)

10. B. Coriton, A. M. Steinberg, J. H. Frank, High-speed tomographic PIV and OH-PLIF measurements in reactive flows, 8th US National Combustion Meeting, IF02, Park City UT (2014)

References

[1] G. Damköhler, *Z. Elektrochem* 46 (1940) 601–652.

[2] D. Garcia, *Computational Statistics and Data Analysis* 54 (6) (2010) 1167–78.

[3] W. Xu, A. Wickersham, L. Ma, *Applied Optics* 54 (9) (2015) 2174–82.

[4] J. Floyd, P. Geipel, A. Kempf, *Combustion and Flame*.

[5] J. Moeck, J. Bourgouin, D. Durox, T. Schuller, S. Candel, *Experiments in Fluids* 54 (1498).

[6] P. Trunk, I. Boxx, C. Heeger, W. Meier, B. Böhm, A. Dreizler, *Proceedings of the European Combustion Meeing* 34 (2) (2013) 3565–72.

[7] R. Wellander, M. Richter, M. Aldén, *Experiments in Fluids* 55 (1764).

[8] A. Steinberg, J. Driscoll, S. Ceccio, *Experiments in Fluids* 44 (2008) 985–99.

[9] A. Stella, G. Guj, J. Kompenhans, H. Richard, M. Raffel, *Aerospace Science Technology* 5 (2001) 357–64.

[10] N. Fukushima, M. Katayama, Y. Naka, T. Oobayashi, M. Shimura, Y. Nada, *Proceedings of the Combustion Institute* 35 (2014) 3009–17.

[11] P. Yeung, S. Pope, *Journal of Computational Physics* 79 (1988) 373–416.